Published in final edited form as:
Proteins. 2011 November ; 79(11): 3132–3143. doi:10.1002/prot.23142.

The Structure, Molecular Dynamics, and Energetics of Centrin-Melittin Complex†

Liliana del Valle Sosa[§], **Elisa Alfaro**[§], **Jorge Santiago**[§], **Daniel Narváez**[§], **Marie Cely Rosado**[§], **Aslin Rodríguez**[§], **Ana María Gómez**[§], **Eric R. Schreiter**[‡,§], and **Belinda Pastrana-Ríos**[*,‡,§]

[‡]Protein Research Center, University of Puerto Rico, Mayagüez Campus, Mayagüez, PR 00681-9019, USA

[§]Department of Chemistry, University of Puerto Rico, Mayagüez Campus, Mayagüez, PR 00681-9019, USA

Abstract

Centrin is a calcium binding protein belonging to the EF-hand superfamily. As with other proteins within this family, centrin is a calcium sensor with multiple biological target proteins. We chose to study *Chlamydomonas reinhardtii* centrin (*Cr*cen) and its interaction with melittin (MLT) as a model for calcium binding protein complexes due to its amphipathic properties. Our goal was to determine the molecular interactions that lead to centrin-MLT complex formation, their relative stability, and the conformational changes associated with the interaction, when compared to the single components. For this, we determined the thermodynamic parameters that define *Cr*cen-MLT complex formation. Two-dimensional infrared (2D IR) correlation spectroscopy were used to study the amide I', I'*, and side chain bands for ^{13}C-*Cr*cen, MLT, and the ^{13}C-*Cr*cen-MLT complex. This approach resulted in the determination of MLT's increased helicity, while centrin was stabilized within the complex. Herein we provide the first complete molecular description of centrin-MLT complex formation and the dissociation process. Also, discussed is the first structure of a calcium binding protein-MLT complex by X-ray crystallography, which shows that MLT has a different binding orientation than previously characterized centrin-bound peptides. Finally, all of the experimental results presented herein are consistent with centrin maintaining an extended conformation while interacting with MLT. The molecular implications of these results are: (1) the recognition of hydrophobic contacts as requirements for initial binding, (2) minimum electrostatic interactions within the C-terminal end of the peptide, and (3) van der Waals interactions within MLT's N-terminal end are required for complex formation.

Centrin is a highly conserved calcium binding protein (CaBP) belonging to the EF-hand superfamily (1–2). Like all EF-hand proteins, centrin responds to cellular Ca^{2+} influx by selectively binding Ca^{2+} at four helix-loop-helix motifs. Unique features of centrin include an additional 20 amino acid residues within the N-terminal domain and an additional four residues at the C-terminal end. Centrin is found in all eukaryotes and is localized to the centrioles and nucleus in vertebrates; to the nucleus-basal body connectors, distal striated fibers, and the flagellar apparatus in green algae; and to the spindle pole body in yeast (3–5).

†This project is supported by NIH-COBRE Grant P20 RR16439-01 (B.P.R.), NIH-SCORE Grant SO6GM08103-38 (B.P.R.) and the Henry Dreyfus Teacher Scholar Award (B.P.R.) at the University of Puerto Rico.

[*]**Correspondence to:** Belinda Pastrana-Rios University of Puerto Rico, Mayagüez Campus, Mayagüez, PR 00681-9019, USA. belinda@hpcf.upr.edu, belinda.pastrana@gmail.com.

Centrin has been proposed to behave as two independent domains (6–8). The C-terminal domain plays a regulatory role that is dependent on the calcium binding state, while the N-terminal domain imparts stability and directs localization (6,9–10). *Chlamydomonas reinhardtii* centrin (*Cr*cen) (Swiss Protein Database accession number P05434) is highly stable (T_m 112.1°C) (11) and has been well characterized in the presence and absence of cations using FT-IR (7,12), CD (12,13), and NMR (6,13) spectroscopies. Holo-*Cr*cen is composed of 60.0% helical, with smaller proportions of β-sheet (12.0%) and β-turn or loops (14.7%), while apo-*Cr*cen is 53.5%-helical, 36.4% β-sheet, and 3.1% β-turn or loops. The vibrational mode at 1650 cm^{-1}, assigned to the π-helix motif, serves as a probe for the dynamics of the C-terminal end.

Melittin (MLT) has been used as a model peptide for the study of CaBP-peptide interactions (14–19). This amphipathic peptide from bee venom (*Apis mellifera*) is composed of 26 amino acids (GIGAILKVLATGLPTLISWIKNKRKQ), of which the first 20 are primarily hydrophobic in nature, while the C-terminal end is positively charged. MLT has recently been the focus of clinical applications resulting in a targeted approach to tumor treatment (20–22) because of its inhibitory effect on tumor growth and its cytotoxicity (23,24). This peptide has also been found to act as a potent inhibitor of calmodulin (CaM) activity.

Prior studies of holo-CaM-MLT (1:1 molar ratio) (14,15,17–19) have reported a dissociation constant (K_d) in the low nanomolar range (14,15,17), whereas the binding of MLT to apo-CaM is much weaker (K_d ~10 μM) (17,18). Creascu's group (16,25) has reported that the human centrin 2 (*Hs*cen2)-MLT complex (1:1 molar ratio) has a K_d of 62.5 nM, while the human centrin 3-MLT complex affinity is 2–3 fold higher.

CaBP-MLT complexes have historically been resistant to high resolution structure determination. However, in an attempt to further explore the mechanism of CaBP binding and its relationship to target specificity and affinity, we have managed to determine a structure of the *Cr*cen-MLT complex by X-ray crystallography. This manuscript is a report of the structural features of the complex, the thermodynamics governing complex formation, and the molecular mechanism of binding and dissociation.

MATERIALS & METHODS

Preparation of protein and peptide samples

Unlabeled *Cr*cen was bacterially expressed, isolated and purified as described in Pastrana-Rios et al. (12). For the FT-IR studies, newly transformed *Escherichia coli* BL21 (DE3) STAR cells from Stratagene with a pT7-5 *Cr*cen recombinant were grown in a 300 mL culture using Spectra 9 ^{13}C-enriched minimal media from Cambridge Isotope Laboratories, Inc. (Andover, MA), in the presence of 50 μg/mL of ampicillin in an orbital shaker at 37 °C and 250 rpm. This inoculum was then added to a 3 L culture with the above mentioned media in a Bioflo 3000 fermentor from New Brunswick Scientific (Edison, NJ) at 300 rpm and 37 °C. Bacterial cell growth was monitored by pelleted cell volume and protein expression induced with IPTG once the cells entered log phase. The bacterial culture was then harvested by centrifugation and subsequently purified following the above mentioned procedure. The protein samples were analyzed by SDS-PAGE and were sent for partial amino acid sequencing and TOF ESI MS before continuing with the biophysical studies. The concentration of each protein was determined using its predicted molar extinction coefficient (M^{-1} cm^{-1}): *Cr*cen ε_{280} = 1,490 and MLT ε_{280} = 5,500. The MLT peptide (Ac-GIGAILKVLATGLPTLISWIKNKRKQ-NH_2) was purchased from Abgent, Inc. (San Diego, CA) and was subjected to extensive dialysis against 0.1 N HCl to remove the inherent TFA present in the sample as a byproduct of the solid phase synthesis. The peptide sample was then subjected to a second dialysis against 50 mM Hepes, 150 mM NaCl, 4 mM

$MgCl_2$, and 4 mM $CaCl_2$ at pH 7.4 and lyophilized repeatedly (6×), while re-dissolving the sample in D_2O (99 at. %D) to ensure complete H→D exchange and removal of the TFA (26). The purified MLT sample was then analyzed by FT-IR spectroscopy to evaluate the extent of the removal of TFA, which would be observed as a sharp band at 1674 cm^{-1}. The MLT sample was judged to be TFA-free.

Calorimetric binding assay

Isothermal titration calorimetry was used to study the interaction between *Cr*cen and MLT. The experiment was performed on a MicroCal VP-ITC microcalorimeter from GE Healthcare Piscataway, NJ. A solution of 120 μM MLT in 50 mM Hepes, 150 mM NaCl, 4 mM $CaCl_2$ and 4 mM $MgCl_2$ at pH 7.4 and 25 °C was sequentially injected into a sample cell containing 10 μM *Cr*cen in the same buffer. Thermodynamic data were fit to a one-site binding model in the MicroCal Origin software to determine the binding constants.

FT-IR spectroscopy

The protein samples were dialyzed under the desired conditions and then lyophilized repeatedly to H→D exchange the sample as mentioned above. A 25 μL aliquot of 60 mg/mL protein in 50 mM Hepes, 150 mM NaCl, 4 mM $MgCl_2$, and 4 mM $CaCl_2$ at pD 6.6 was deposited on a 49 × 4 mm custom milled CaF_2 window with a fixed path length of 40 μm. A reference cell was prepared similarly, and both cells were set in a custom dual chamber cell holder. The temperature within the cell was controlled *via* a Neslab RTE-740 refrigerated bath (Thermo Electron Corp., NH) and monitored with a thermocouple positioned in close contact with the sample. The temperature accuracy was estimated to be within 1 °C. Routinely, spectral data acquisition was performed at the desired preset temperature with 10 min. intervals, once the temperature in the cell was reached, to allow for thermal equilibrium of the sample. The instrument used was a Jasco FT-IR Spectrophotometer model 6200 (Jasco Corporation, Tokyo, Japan) equipped with an MCT detector, a sample shuttle and interface. Typically, 512 scans were co-added, apodized with a triangular function, and Fourier transformed to provide a resolution of 4 cm^{-1} with the data encoded every 2 cm^{-1}.

Spectral analysis

FT-IR spectroscopy provides protein conformational dynamics. Particularly, the amide I' band typically observed within 1700–1600 cm^{-1} is characteristic of peptide bonds within a protein, comprised mainly of highly coupled carbonyl stretching modes (ν(C=O)) that are sensitive to the conformation of the protein. H-D exchange simplifies the underlying spectral contributions within the amide I' and II bands as follows. The N-D deformation modes of the peptide bonds within the amide II band (1550 cm^{-1}) shift ~100 cm^{-1} to lower wavenumbers, to the amide II' band (1450 cm^{-1}). As a result, the band observed within 1600–1500 cm^{-1} is comprised of the side chain modes and it is thus assigned; therefore the H→D exchange effectively reduces the number of contributing vibrational modes, without sacrificing structural and dynamic information about the behavior of the protein (7,12,26–34). In addition, uniformly ^{13}C-labeling one of the protein components results in a shift of all the carbon containing vibrational modes to lower wavenumbers, effectively separating the ν(^{12}C=O) vibrations (amide I' band at 1645 cm^{-1}) for one protein (e.g., MLT) from the ν(^{13}C=O) vibrations (amide I'* band at 1596 cm^{-1}) for the other (e.g., centrin). This strategy allows for the simultaneous study of both protein components (26). Also, the ^{13}C-carboxylate stretching vibrations for aspartates and glutamates shift to lower wavenumbers by ~30cm^{-1}, thus simplifying the contributions within the amide I'* band. Furthermore, these shifts to lower wavenumbers due to heavy isotope incorporation can be predicted for stretching modes by assuming a simple harmonic oscillator, enabling secondary structure assignment.

2D IR correlation spectroscopy is a technique derived from NMR and developed by Noda (35–36). It uses the FT-IR series of sequential spectra as a function of a perturbation (temperature, H/D exchange, ligand titration, etc.) to generate the synchronous and asynchronous plots. In general, the analysis spreads the acquired spectral data in two dimensions, thus enhancing the spectral resolution in the synchronous plot and providing temporal information on the molecular events that occur in the asynchronous plot (7,12,26,31, 34–37). Both plots provide information on the correlation between vibrational modes within the spectral region of interest (1720–1490 cm^{-1}). Consequently, this technique is sensitive to backbone vibrational modes as well as certain side chain modes (i.e., arginine, aspartates, and glutamates) being perturbed and, as a result, one can identify changes in these modes as a function of the perturbation.

For the FT-IR spectral analysis, the spectral data was not manipulated except for baseline correction. The spectral overlay, peak pick routines, and 2D IR correlation spectroscopy analysis were performed using a Kinetics program for MATLAB (MathWorks, Natick, MA) generously provided by Dr. Erik Goormaghtigh from the Free University of Brussels, Belgium. The thermal dependence plots were generated using Origin version 7 from OriginLab Corp., Northampton, MA.

Crystallography

Crystals were grown using the hanging drop vapor diffusion method at room temperature by mixing 2 μL of the *Cr*cen-MLT (1:1.5 molar ratio) solution with 2 μL of a precipitant solution containing 50 mM HEPES, pH 7.5, 0.2 M KCl, and 40% v/v pentaerythritol propoxylate (5/4 PO/OH). Crystals appeared as clusters of colorless needles after 2–5 days. A single crystal measuring ~400×40×20 μm was separated from a cluster and directly mounted at 93 K in a fiber loop for data collection. X-ray diffraction data were collected to 2.2 Å resolution on a rotating copper anode source with a Saturn92 CCD detector (MSC) and integrated/scaled using the HKL software suite (Table 1). The structure was solved by molecular replacement in the space group $P2_12_12$ using the program Phaser (38) and searching sequentially for the N- and C-terminal domains of bovine CaM (Protein Data Bank entry 1CDM). The previously determined structure of the MLT peptide (PDB ID 2MLT) was used to add the MLT peptide into difference density. Strong positive peaks at the expected calcium ion positions in the F_o–F_c electron density map, calculated using phases from the molecular replacement model (from which calcium ions had been removed), confirmed the correctness of the solution. Rebuilding and refinement of the model was done using Coot (39,40) and Refmac5 (41) from the CCP4 program suite (42). The final structure contains residues 20–164 of *Cr*cen and the first 20 amino acids of MLT, as well as 4 calcium ions and 23 water molecules. The PDB ID for this complex is 3QRX. The model refined to an R-factor of 29.41% and R-free of 34.1% (Table 1), values significantly higher than expected for a structure at this resolution (2.30 Å resolution). Extensive efforts were made to improve the model further by collection of new datasets from additional crystals, reprocessing of the data, refinement in a lower-symmetry space group, and model-bias removal were applied, but they were unsuccessful. Although composite-omit electron density maps generally support the features of the model presented here, we have refrained from a more detailed analysis of the crystal structure due to the high R-factors.

RESULTS & DISCUSSION

Molecular species

SDS-PAGE of *Cr*cen revealed a single protein with an approximate molecular weight of 20 kDa (Figure 1A). MLT and *Cr*cen (Figure 1B and C) were determined to be in their monomeric forms, and MLT's empirical m/z value of 2,889.6 agreed with the calculated m/z

ratio. The experimentally determined m/z ratios for ^{13}C-*Cr*cen were 20,004.3 which indicates >99.4% ^{13}C isotope incorporation. The parent peak at 20,004.3 m/z also exhibits two shoulders at lower m/z values due to differences in Ca^{2+} binding. Also considered is the loss of the methionine residue at the amino terminal end as evidenced from partial amino acid sequencing. The protein sample was dialyzed against the appropriate buffer to ensure the holo state of centrin.

Thermodynamics of the Crcen-MLT complex

The interaction between *Cr*cen and MLT was determined by calorimetry to be exothermic at 25 °C, with a dissociation constant K_d = 7.41 ± 0.07 nM, n = 1.38 ± 0.01, ΔH_b = −2.73 ± 0.07 kcal/mol, and ΔS = 28.0 cal/mol•K, resulting in ΔG = −11.1 kcal/mol. Several MLT-CaBP complexes have been reported in the PINT database (43) or are directly cited herein (14–19), two of which are summarized in Figure 2 along with *Cr*cen-MLT. The *Cr*cen-MLT complex was the most stable complex. *Cr*cen-MLT exhibits the highest affinity for MLT when compared to CaM-MLT (14,18) and *Hs*cen2-MLT complexes (16), also the contributing enthalpy change observed for Hscen2-MLT is much more favorable for binding than in *Cr*cen-MLT and CaM-MLT. Complex formation is driven by entropy for *Cr*cen-MLT and CaM-MLT complexes.

Thermal dependence studies

We compared the FT-IR spectra in the spectral region of 1720–1390 cm^{-1} (the amide I', I'*, side chain, and amide II' bands) within the temperature range of 5–95 °C in the presence of Ca^{2+} and Mg^{2+} for MLT, ^{13}C-*Cr*cen, and the ^{13}C-*Cr*cen-MLT complex (Figure 3A–C), suggesting all protein samples were fully H-D exchanged by the intensity ratio of the amide II' and I' or amide II' and I'* band.

The position of the peak maxima for the amide I' band for MLT, the amide I'* band for ^{13}C-*Cr*cen, and the amide I'* band for the ^{13}C-*Cr*cen-MLT complex are plotted as a function of temperature (Figure 4). For the pure components (Figure 4A) a trend of increasing frequency with temperature resulted in a shift of 7 cm^{-1} for MLT, but only 3.5 cm^{-1} for ^{13}C-*Cr*cen. The magnitude of the change of the backbone associated frequencies (ν(C=O) and ν(^{13}C=O) for MLT and centrin, respectively) may be indicative of the relative stability of these two protein components. The magnitude of the shift for ^{13}C-*Cr*cen is similar to that of unlabeled *Cr*cen (2.5 cm^{-1}) (12). Yet, for the complex (Figure 4B) a cooperative effect was observed within the temperature range of 5–60 °C, with a shift from 1603.3 to 1600.8 cm^{-1} resulting in 2.4 cm^{-1}, suggesting the complex is being stabilized and that the molecular changes observed within this temperature range may define complex formation. In contrast, for the temperature range of 60–95 °C, the complex is being destabilized due to the increase in temperature resulting in a shift of 2.0 cm^{-1}. *Cr*cen is in the holo state, thus ensuring its transition temperature at 112.1 °C; therefore the molecular changes described within the 60–95 °C temperature range are events that lead to but do not include thermal denaturation of centrin. Furthermore, no aggregation bands are present in the spectra within the entire temperature range studied. A similar stability characterizes the *Cr*cen-MLT complex, thus these experiments effectively separate complex formation from thermal unfolding and allow the former to be analyzed.

Band assignments

Contributing backbone vibrational modes within the FT-IR spectral overlay and 2D IR correlations are summarized below for the amide I' and I'* bands (1720–1550 cm^{-1}) and side chain band (1550–1490 cm^{-1}). In general, all spectral data sets are arranged in columns and the similar plot types are arranged in rows to facilitate comparison and analysis.

The band assignments were done with baseline-corrected spectra for the single components (MLT or ^{13}C-*Cr*cen). These assignments were also used in the complex spectra and the 2D IR correlation spectroscopy analysis to facilitate interpretation and comparison. Furthermore, the assignments have been validated by two of three means: (1) by previous work as cited, (2) the X-ray structure reported herein, or (3) by simulated spectra (*results not shown*). Several spectral overlays within 1720–1490 cm^{-1} for the full temperature range 5–98 °C are shown in Figure 5. For MLT (Figure 5A), the amide I' band comprises: a "kink" (1670.2 cm^{-1}), presumably due to the proline (P_{14}), random coil (1656.1 cm^{-1}) (26), and β-strand (1628.0 cm^{-1}). The weak side chain band is composed of arginine (R_{24}) stretching modes (1606.0 and 1582.2 cm^{-1}). For ^{13}C-*Cr*cen (Figure 5B) the amide I'* band rendered the following assignments: loops (1630.0 and 1637.0 cm^{-1}), π-helix (1624.0 cm^{-1}) at the C-terminal end of the sequence, α-helical contributions (1614.0 cm^{-1}), and β-sheets (1597.3 cm^{-1}) present as short segments found within the calcium binding sites (consistent with the X-ray structure reported herein). The side chain band consisted of the aspartates (1538.0 cm^{-1}), glutamates (1519.1 cm^{-1}), and different stretching modes within the guanidinium of the arginine residues: ^{13}C-N stretching modes (1572.4 and 1554.0 cm^{-1}) stretching modes (1608.2 and 1582.3 cm^{-1}) consistent with our previous studies (7,11,12,26). For the ^{13}C-*Cr*cen-MLT complex (1:2 molar ratio) shown in Figure 5C, the amide I' and I'* bands are composed of MLT's "kink" (1670.7 cm^{-1}), random coil contribution (1656.3 cm^{-1}), a new band associated with a 3_{10}-helical component (1641.2 cm^{-1}) and concomitant loss of the β-strand at 1628.0 cm^{-1} (30). For the ^{13}C-*Cr*cen within the complex, β-sheet (1597.0 cm^{-1}), π-helix (1624.0 cm^{-1}), and loops (1630.0 and 1637.0 cm^{-1}) were observed and are consistent with the X-ray structure reported herein. Limited to the side chain band are the following vibrational modes including the symmetric stretch of the guanidinium in the exchanged arginine (1582.3 cm^{-1}) arising from both components and the ^{13}C-N antisymmetric and symmetric stretches (1572.4 and 1554.0 cm^{-1}, respectively) exclusive to ^{13}C-*Cr*cen. Also observed within the side chain band are the ^{13}C-carboxylate modes for the glutamates (1519.1 cm^{-1}) and aspartates (1538.0 cm^{-1}) (44).

2D IR correlation spectroscopy

2D IR correlation spectroscopy enhances the resolution of the spectral region of interest via the synchronous plot and provides the temporal order of events that occurs during the perturbation via the asynchronous plot. The auto peaks found in the synchronous plots show changes in intensity with peaks that are in phase, while the asynchronous plots are composed of peaks that change in intensity out of phase from each other. The phase information in the asynchronous plot is used to interpret the order of events, i.e., to determine whether the change in ν_1 or ν_2 occurs first, according to Noda's rules (35,36).

The synchronous plots for the single components (MLT and ^{13}C-*Cr*cen) studied within the spectral region 1720–1490 cm^{-1} are shown in Figure 5D and E, respectively. In each case, a spectral region (for MLT, 1600–1540 cm^{-1}, and for ^{13}C-*Cr*cen, 1720–1650 cm^{-1}) is observed to have little or no overlap. The auto and cross peaks with their band assignments are consistent with the band assignments presented above for the same spectral region. The auto peak with the greatest intensity change for MLT (Figure 5D) was the random coil (1656 cm^{-1}). For ^{13}C-*Cr*cen (Figure 5E) the auto peak with the greatest intensity change was the β-sheet (1597 cm^{-1}). These same auto peaks are observed to have the greatest intensity changes within the complex (Figure 5F) with the corresponding cross peaks suggesting a *Cr*cen-MLT interaction.

Evidence of Centrin-MLT interaction

The correlated cross peaks with strong intensity changes suggest the existence of an interaction between centrin and MLT. In the synchronous plot (Figure 5F), the changes in

intensity are in phase with one another and involve MLT's β-strand (1628.0 cm^{-1}) with ^{13}C-*Cr*cen's β-sheets (1597 cm^{-1}). MLT's β-strand (1628.0 cm^{-1}) is also interacting with ^{13}C-*Cr*cen's glutamates (1519 cm^{-1}). These interactions suggest that the C-terminal end of MLT adopts a β-strand conformation due to the polar and basic amino acid composition within this segment of the sequence. This would allow for the electrostatic, ionic or hydrogen-bonding interactions observed for ^{13}C-*Cr*cen's glutamates and aspartate (presumably within the loop within the third and fourth EF-hands located in C-terminal domain) and MLT's carboxyl terminal end. These interactions would affect the transition dipole moments observed for the vibrational modes discussed, causing the intensity changes and peak shifts observed.

In the asynchronous plot (Figure 5I), where changes in cross peak intensity are out of phase from one another, we observed several strong correlations: MLT's random coil (1656.0 cm^{-1}) with ^{13}C-*Cr*cen's π-helix (1624.1 cm^{-1}) and β-sheets (1597 cm^{-1}), and MLT's random coil (1656.0 cm^{-1}) and MLT's "kink" (1670.6 cm^{-1}) with its own β-strand (1628.0 cm^{-1}). Furthermore, ^{13}C-*Cr*cen's π-helix (1622.1 cm^{-1}) correlates with MLT's only Arg_{24} (1578 cm^{-1}). MLT's α-helical motif (1641 cm^{-1}) correlate with ^{13}C-*Cr*cen's glutamates (1525 cm^{-1}) (located within the loop region and the contiguous helices within the C-terminal domain). Consequently, MLT undergoes conformational changes upon interaction with centrin that are not observed for the pure components.

Molecular events for the single components

(MLT and ^{13}C-*Cr*cen) within the spectral region 1720–1490 cm^{-1} were studied using the synchronous (Figure 5D and E) and asynchronous (Figure 5G and H) plots. The schematic diagram (Scheme 1A and B for MLT and ^{13}C-*Cr*cen, respectively) lists the band assignments and arranges them in the order in which they were perturbed, reflecting the relative stability associated with each vibrational mode. For MLT, the random coil (1656 cm^{-1}) was the least stable followed by the β-strand (1628.0 cm^{-1}) and the "kink" (1670 cm^{-1}) located near the center of the sequence. Finally the single Arg residue at position 24 is perturbed, thus serving as a probe for the C-terminal end of the peptide. Consequently, the C-terminal end of MLT is the most stable portion of the peptide and is presumably stabilized by hydrogen bonding interactions with its aqueous environment. These results are consistent with those by Dr. Prendergast group using NMR spectroscopy (45–47).

For ^{13}C-*Cr*cen, all the calcium binding sites (I–IV) are bound to Ca^{+2} (see the structural information below), therefore the glutamates and aspartates within this sequence are also stable due to their coordination with the calcium ion. This translates stability to the majority of the α-helical motifs present in the protein. Therefore, it is not surprising to observe small changes in the transition dipole moments associated with this vibrational mode (1614 cm^{-1}), and as a result a small intensity change is observed for this cross peak. Furthermore, additional glutamates and aspartates are located within the loops (1630 and 1637 cm^{-1}) that connect the EF-hand motifs at each terminal end; however, the sequence composition is different for these two loops. The N-terminal loop (1630 cm^{-1}) is composed of lysines and other polar residues which can interact with nearby glutamates by hydrogen bonding or intra-salt bridge interactions, thereby stabilizing this structural motif (48,49). The loop (1637 cm^{-1}) located at the C-terminal domain does not have the possibility of being stabilized by these weak interactions with neighboring residues, but instead are stabilized by interactions with the aqueous environment and is therefore more stable. The first perturbation events involve the glutamates (1519 cm^{-1}) in this C-terminal domain loop followed by the aspartates (1538 cm^{-1}). The perturbation of these residues with their associated electrostatic interactions have a long range effect on the short β-sheets (1597 cm^{-1}) located within the calcium binding sites causing them to be perturbed. The associated arginine vibrational modes within the guanidinium are then perturbed (1554, 1582, and 1572 cm^{-1}) followed by

the α-helical motifs (1614 cm^{-1}), the π-helix (1624 cm^{-1}) located at the C-terminal end, and finally, the loops (1630 and 1637 cm^{-1}). The order of events presented for *Cr*cen is in accord with previously published work for the unlabeled protein (12).

Molecular description of complex formation

By separating the spectral data sets for ^{13}C-*Cr*cen-MLT complex shown in Figure 5C, as indicated by the thermal dependence plot shown in Figure 4B within the temperature range of 5 – 60°C, we can describe the molecular events that define the cooperative behavior observed during complex formation (Figure 6A, C and E). These results have been summarized by using the band assignments for each protein component within the complex (Scheme 2A). Briefly, centrins' glutamates (1519 cm^{-1}) perturb MLT's random coil (1656 cm^{-1}) causing a conformational change in MLT, which adopts a 3_{10}-helix (1641 cm^{-1}). This helical conformation allows for weak interactions with centrins' aspartates (1538 cm^{-1}). The center portion of MLT is then perturbed within the "kink" region (1670 cm^{-1}). These cumulative perurbations then affect the C-terminal domain loop (1637 cm^{-1}) of centrin. Then, centrin's N-terminal domain loop (1630 cm^{-1}) is perturbed followed by the guanidinium (1554 cm^{-1}) symmetric stretching mode of centrin's arginines. These events are followed, by centrins' helical motifs being perturbed (π- and α-helix, at 1624 and 1614 cm^{-1}, respectively), while the short β-sheet segments (1597 cm^{-1}) located within the calcium binding sites are stabilized; presumably by long range electrostatic interactions involving MLT's C-terminal end sequence and centrin's C-terminal domain loop. Finally, arginine stretching modes (1572 cm^{-1} and 1582 cm^{-1} for $\nu_a(^{13}C\text{-}N)$ and ν_s(N-D), respectively) within centrin are perturbed, therefore representing the most stable component. The high stability of centrins arginines within the complex when compared to pure centrin is presumably due to hydrogen bonding interactions with its aqueous environment (Arg located at the N-terminal domain, tethered helix) and with MLT backbone carbonyls and glutamine residue located in the C-terminal end of the peptide (Arg located within centrins C-terminal domain i.e., loop and π-helix). Similarly, the single arginine and neighboring lysines within the MLT sequence located within the C-terminal end are stabilized by salt-bridge or electrostatic interactions with centrin's glutamates (Glu^- at position 136, 137, 138, 141 and 145) located within the C-terminal domain loop or by hydrogen bonding interaction with the Ser_{167} or Thr_{166} within the π-helix.

Thermally induced complex dissociation

The spectral data set for the temperature range of 60 – 95°C is shown in Figure 6B and was similarly selected after analyzing the thermal dependence plot shown in Figure 4B. We can describe the molecular events that define the dissociation of the ^{13}C-*Cr*cen-MLT complex by using the 2D IR correlation spectroscopy shown in Figure 6D and F, also summarized in a schematic form based on the band assignments (Scheme 2B). The least stable region within the complex is MLT's "kink" (1670 cm^{-1}) at Pro_{14}. The level of flexibility in this region is greater than that of the random coil (1656 cm^{-1}) segments within the peptide (MLT). The fluctuations described in MLT along with the rising temperature perturb centrins' β-sheets (1597 cm^{-1}), followed by arginines' guanidinum's N-D asymmetric stretch (1608 cm^{-1}) and centrins' glutamates (1519 cm^{-1}). They are presumably perturbed, by the breakage of any salt-bridge or ionic interaction between these residues within the complex, causing a loss of the 3_{10}-helical motif in MLT. The arginine guanidinum N-D symmetric stretch (1582 cm^{-1}) is then perturbed. These cumulative perturbations; affect centrin's α-helical components (1614 cm^{-1}) and the C-terminal domain loop (1637 cm^{-1}). These perturbations along centrin and the rise in temperature cause the intra-molecular salt-bridge interactions to break within the aspartates (1538 cm^{-1}) and arginines, represented by the guanidinium ^{13}C-N stretching vibrations (1572 and 1554 cm^{-1}, in that order). Also considered are the perturbations of weak interactions between centrin arginines (^{13}C-N

stretching vibrations) located within the π-helix and MLT's backbone carbonyls or the glutamine residue located at the C-terminal end. The final perturbation events and as a result the most stable structural motifs within the complex, are centrins' N-terminal domain loop (1630 cm^{-1}) and the π-helix (1624 cm^{-1}) found at the C-terminal end of centrin. The high stability of these motifs correlates with the most stable motifs found in the pure ^{13}C-*Cr*cen and significantly differs from the elucidated order events for the formation of the complex. Thus, describing the dissociation of the complex.

X-ray crystal structure of the Crcen-MLT complex

*Cr*cen adopts an extended dumbbell-shaped conformation in the crystal structure (Figure 7), with Ca^{2+} ions occupying all four EF-hands and both the N- and C-terminal domains in the open conformation. As in the structure of *Hs*Cen2 bound to XPC peptide (PDB ID 2GGM) (50), the helical MLT peptide interacts with the C-terminal domain of *Cr*cen. However, the orientation of the bound peptides relative to the centrin molecule differs. The N-terminal end of MLT is oriented towards the *Cr*cen tethered helix. The MLT helix is bent due to the presence of proline at position 14, as was observed in a previous structure of MLT alone (PDB ID 2MLT) and does not interact as closely with *Cr*cen as other peptides have been observed to interact with related EF-hand proteins. It arches over the exposed hydrophobic binding surface of the C-terminal domain, making a few Van der Waals contacts near the beginning of the MLT helix (Figure 7). Indeed, the large pocket in centrin filled by XPC's tryptophan in the *Hs*Cen2-XPC and yeast centrin-Kar1p structures remains empty in the *Cr*cen-MLT structure.

CONCLUSIONS

The value of an interdisciplinary and comparative approach for understanding the complex molecular behavior of proteins and their interactions has been proven in the work presented here. This approach is essential to understanding the role of proteins and their biological function. Isothermal titration calorimetry provided the thermodynamic profile of a stable complex driven entropically, while the vibrational spectroscopy and 2D IR correlation spectroscopy analysis was essential for a dynamic molecular description of both protein components during their interaction. The results presented for the *Cr*cen-MLT complex were compared to the pure components, providing further evidence of the effects of stabilization of centrin when interacting with the MLT. Long range electrostatic interactions were observed between centrin's C-terminal domain loop and the short β-sheets found at the calcium binding sites III and IV. Meanwhile, the electron density map rendered hydrophobic and van der Waals interactions between the N-terminal end of the peptide and centrins' tethered helix towards the C-terminal domain and arches over the hydrophobic surface within the EF-hand. The centrin molecule, however, remained in its extended conformation, potentially due to MLT not having the required polar residues within its sequence, specifically between A_4 and L_{16}, to induce the large conformational change observed for other centrin-target complexes. Finally, with the novel structural information provided, we have confirmed that the MLT peptide limits its interaction to the C-terminal domain of centrin, while maintaining an extended structure within the complex. The cumulative results presented herein provide a detailed description of the *Cr*cen-MLT complex.

Abbreviations

***Cr*cen**	*Chlamydomonas reinhardtii* centrin
MLT	melittin
CaBP	calcium binding protein

IPTG	isopropyl β-D-thiogalactopyranoside
SDS-PAGE	sodium dodecyl sulfate-polyacrylamide gel electrophoresis
TOF-ESI MS	time of flight electrospray mass spectrometry
MALDI MS	matrix assisted laser desorption ionization mass spectrometry
FT-IR	Fourier transform infrared
2D IR	two-dimensional infrared
ITC	isothermal titration calorimetry

Acknowledgments

The authors would like to thank Dr. Michael Berne from the Mass spectrometry facility at Tufts medical school for performing the MS analysis and partial amino acid sequencing on centrin and Dr. Melissa Stauffer of Scientific Editing Solutions for editing the manuscript.

REFERENCES

1. Kretsinger RH. Calcium-binding proteins. Annu. Rev. Biochem. 1976; 45:239–266. [PubMed: 134666]
2. Nakayama S, Moncrief ND, Kretsinger RH. Evolution of EF-hand calcium-modulated proteins. II. Domains of several subfamilies have diverse evolutionary histories. J. Molec. Evol. 1992; 34:416–448. [PubMed: 1602495]
3. Laoukili J, Perret E, Middendorp S, Houcine O, Guennou C, Marano F, Bornens M, Tournier F. Differential expression and cellular distribution of centrin isoforms during human ciliated cell differentiation in vitro. J. Cell Sci. 2000; 113(Pt 8):1355–1364. [PubMed: 10725219]
4. Nishi R, Okuda Y, Watanabe E, Mori T, Iwai S, Masutani C, Sugasawa K, Hanaoka F. Centrin 2 stimulates nucleotide excision repair by interacting with xeroderma pigmentosum group C protein. Mol. Cell Biol. 2005; 25:5664–5674. [PubMed: 15964821]
5. Salisbury JL. A mechanistic view on the evolutionary origin for centrin-based control of centriole duplication. J. Cell Physiol. 2007; 213:420–428. [PubMed: 17694534]
6. Hu H, Chazin WJ. Unique features in the C-terminal domain provide caltractin with target specificity. J. Mol. Biol. 2003; 330:473–484. [PubMed: 12842464]
7. Ortiz M, Sanoguet Z, Hu H, Chazin WJ, McMurray CT, Salisbury JL, Pastrana-Rios B. Dynamics of Hydrogen-deuterium exchange in *Chlamydomonas* centrin. Biochemistry. 2005; 44:2409–2418. [PubMed: 15709753]
8. Veeraraghavan S, Fagan PA, Hu H, Lee V, Harper JF, Huang B, Chazin WJ. Structural independence of the two EF-hand domains of caltractin. J. Biol. Chem. 2002; 277:28564–28571. [PubMed: 12034713]
9. Matei E, Miron S, Blouquit Y, Duchambon P, Durussel I, Cox JA, Craescu CT. C-terminal half of human centrin 2 behaves like a regulatory EF-hand domain. Biochemistry. 2003; 42:1439–1450. [PubMed: 12578356]
10. Sheehan JH, Bunick CG, Hu H, Fagan PA, Meyn SM, Chazin WJ. Structure of the N-terminal calcium sensor domain of centrin reveals the biochemical basis for domain-specific function. J. Biol. Chem. 2006; 281:2876–2881. [PubMed: 16317001]
11. Sanoguet-Carrero Z, Campbell M, Ramos S, Seda C, Pastrana-Rios B. Effects of phosphorylation in *Chlamydomonas* centrin Ser 167. Calcium Binding Proteins. 2006; 1:108–114.
12. Pastrana-Rios B, Ocaña W, Rios M, Vargas GL, Ysa G, Poynter G, Tapia J, Salisbury JL. Centrin: Its Secondary Structure in the Presence and Absence of Cations. Biochemistry. 2002; 41:6911–6919. [PubMed: 12033923]

13. Weber C, Lee VD, Chazin WJ, Huang B. High-level expression in *Escherichia coli* and characterization of the EF-hand Calcium-binding protein caltractin. J. Biol. Chem. 1994; 269:15795–15802. [PubMed: 8195234]
14. Milos M, Schaer J-J, Compte M, Cox JA. Microcalorimetric investigation of the interactions in the ternary complex calmodulin-calcium-melittin. J. Biol. Chem. 1987; 262:2746–2749. [PubMed: 3818620]
15. Cox JA, Compte M, Fitton JE, DeGrado WF. The interaction of calmodulin with amphiphilic peptides. J. Biol.Chem. 1985; 260:2527–2534. [PubMed: 2982823]
16. Durussel I, Blouquit Y, Middendorp S, Craescu CT, Cox JA. Cation-and peptide-binding properties of human centrin 2. FEBS Lett. 2000; 472:208–212. [PubMed: 10788612]
17. Kataoka M, Head JF, Seaton BA, Engelman DM. Melittin binding causes a large calcium-dependent conformational change in calmodulin. Proc. Natl. Acad. Sci.U.S.A. 1989; 86:6944–6948. [PubMed: 2780551]
18. Maulet Y, Cox JA. Structural changes in melittin and calmodulin upon complex formation and their modulation by calcium. Biochemistry. 1983; 22:5680–5686. [PubMed: 6652077]
19. Newman RA, Van Scyoc WS, Sorensen BR, Jaren OR, Shea MA. Interdomain cooperativity of calmodulin bound to melittin preferentially increases calcium affinity of sites I and II. Proteins. 2008; 71:1792–1812. [PubMed: 18175310]
20. Holle L, Song W, Holle E, Wei Y, Li J, Wagner TE, Yu X. *In vitro*-and *in vivo*-targeted tumor lysis by an MMP2 cleavable melittin-LAP fusion protein. Int. J. Oncol. 2009; 35:829–835. [PubMed: 19724919]
21. Park JH, Jeong YJ, Park KK, Cho HJ, Chung IK, Min KS, Kim M, Lee KG, Yeo JH, Park KK, Chang YC. Melittin suppresses PMA-induced tumor cell invasion by inhibiting NF-kappaB and AP-1-dependent MMP-9 expression. Mol. Cells. 2010; 29:209–215. [PubMed: 20082219]
22. Soman NR, Baldwin SL, Hu G, Marsh JN, Lanza GM, Heuser JE, Arbeit JM, Wickline SA, Schlesinger PH. Molecularly targeted nanocarriers 24 deliver the cytolytic peptide melittin specifically to tumor cells in mice, reducing tumor growth. J. Clin. Invest. 2009; 119:2830–2842. [PubMed: 19726870]
23. Orsolic N. Potentiation of bleomycin lethality in HeLa and V79 cells by bee venom. Arh. Hig. Rada Toksikol. 2009; 60:317–326. [PubMed: 19789161]
24. Wang C, Chen T, Zhang N, Yang M, Li B, Lu X, Cao X, Ling C. Melittin, a major component of bee venom, sensitizes human hepatocellular carcinoma cells to tumor necrosis factor-related apoptosis-inducing ligand (TRAIL)-induced apoptosis by activating CaMKII-TAK1-JNK/p38 and inhibiting IkappaBalpha kinase-NFkappaB. J. Biol. Chem. 2009; 284:3804–3813. [PubMed: 19074436]
25. Cox JA, Tirone F, Durussel I, Firanescu C, Blouquit Y, Duchambon P, Craescu CT. Calcium and magnesium binding to human centrin 3 and interaction with target peptides. Biochemistry. 2005; 44:840–850. [PubMed: 15654740]
26. Pastrana-Rios B. Mechanism of Unfolding of a Model Helical Peptide. Biochemistry. 2001; 40:9074–9081. [PubMed: 11478873]
27. Arrondo JLR, Muga A, Castresana J, Goñi FM. Quantitative Studies of the Structure of Proteins in Solution by Fourier-transform infrared spectroscopy. Prog. Biophys. Molec. Biol. 1993; 59:23–56. [PubMed: 8419985]
28. Chirgadze YN, Fedoroy V, Trushina NP. Estimation of amino acid residue side-chain absorption in the infrared spectra of protein solutions in heavy water. Biopolymers. 1975; 14:679–694. [PubMed: 1156632]
29. Venyaminov SY, Kalnin NN. Quantitative IR spectrophotometry of peptide compounds in water (H_2O) solutions 1. Spectral parameters of amino-acid residue absorption-bands. Biopolymers. 1990; 30:1243–1257. [PubMed: 2085660]
30. Fabian, H.; Mantele, W. Encyclopedia of Analytical Chemistry. New Jersey: John Wiley & Sons Ltd.; 2002. Infrared Spectroscopy of Proteins; p. 1-24.
31. Griffith, P.; Haseth, JA. Fourier Transform Infrared Spectroscopy. New Jersey: John Wiley & Sons Ltd.; 2007.

32. Haris PI, Chapman D. The conformational analysis of peptides using Fourier transform IR Spectroscopy. Biopolymers. 1995; 37:251–263. [PubMed: 7540054]
33. Jackson M, Haris PI, Chapman D. Fourier transform infrared spectroscopic of Ca^{2+} binding proteins. Biochemistry. 1991; 30:9681–9686. [PubMed: 1911755]
34. Mantsch, HH. Historical Survey. New York: Marcel Dekker, Inc.; 2001. Historical Survey of Infrared and Raman Spectroscopy of Biological Materials; p. 1-13.
35. Noda I. Advances in two-dimensional correlation spectroscopy. Vibrat. Spectrosc. 2004; 36:143–165.
36. Noda I. Recent advancement in the field of two-dimensional correlation spectroscopy. J. Mol. Struct. 2008; 883:2–26.
37. Ozaki Y, Murayama K, Wu Y, Czarnik-Matusewicz B. Two-dimensional infrared correlation spectroscopy studies on secondary structures and hydrogen bondings of side chains of proteins. Spectrosc. Int. J. 2003; 17:79–100.
38. Otwinowski Z, Minor W. Processing of X-ray Diffraction Data Collected in Oscillation Mode. Methods Enzymol. 1997; 276:307–326.
39. Emsley P, Cowtan K. Coot: model-building tools for molecular graphics. Acta Crystallogr. Biol. D. 2004; 60:2126–2132.
40. Emsley P, Lohkamp B, Scott WG, Cowtan K. Features and development of Coot. Acta Crystallogr. Biol. D. 2010; 66:486–501.
41. Murshudov GN, Vagin AA, Dodson EJ. Refinement of macromolecular structures by the maximum-likelihood method. Acta Crystallogr. Biol. D. 1997; 50:760–763.
42. Collaborative Computational Project, N. The CCP4 Suite: Programs for protein crystallography. Acta Crystallogr.Biol. D. 1994; 50:760–763.
43. Kumar S, Gromiha MM. PINT: Protein-protein interactions thermodynamic database. Nucl. Acids Res. 2006; 34:D195–D198. [PubMed: 16381844]
44. Zhang M, Fabian H, Mantsch HH, Vogel HJ. Isotope-edited Fourier transform infrared spectroscopy studies of calmodulin's interaction with its target peptides. Biochemistry. 1994; 33:10883–10888. [PubMed: 7522050]
45. Buckley P, Edison AS, Kemple MD, Prendergast FG. ^{13}C alpha-NMR assignments of melittin in methanol and chemical shift correlations with secondary structure. J. Biomol. NMR. 1993; 3:639–652. [PubMed: 8111230]
46. Kemple MD, Buckley P, Yuan P, Prendergast FG. Main chain and side chain dynamics of peptides in liquid solution from ^{13}C NMR: Melittin as a model peptide. Biochemistry. 1997; 36:1678–1688. [PubMed: 9048551]
47. Zhu L, Kemple MD, Yuan P, Prendergast FG. N-terminus and lysine side chain pKa values of melittin in aqueous solutions and micellar dispersions measured by ^{15}N NMR. Biochemistry. 1995; 34:13196–13202. [PubMed: 7548083]
48. Marqusee S, Baldwin RL. Helix stabilization by $Glu^{-}\cdots Lys^{+}$ salt bridges in short peptides of de novo design. Proc. Natl. Acad. Sci. U.S.A. 1987; 84:8898–8902. [PubMed: 3122208]
49. Scholtz JM, Qian H, Robbins VH, Baldwin RL. The energetics of ion-pair and hydrogen-bonding interactions in a helical peptide. Biochemistry. 1993; 32:9668–9676. [PubMed: 8373771]
50. Thompson JR, Ryan ZC, Salisbury JL, Kumar R. The structure of the human centrin 2-xeroderma pigmentosum group C protein complex. J. Biol. Chem. 2006; 281:18746–18752. [PubMed: 16627479]

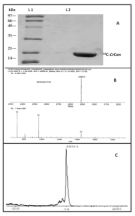

FIGURE 1.

Biochemical characterization of *Chlamydomonas reinhardtii* centrin and MLT. **(A)** SDS-PAGE, **(B)** MALDI MS analysis of MLT also corresponds to its monomeric form, and **(C)** MS analysis of *Cr*cen indicates the protein is ^{13}C-labeled and in its monomeric state.

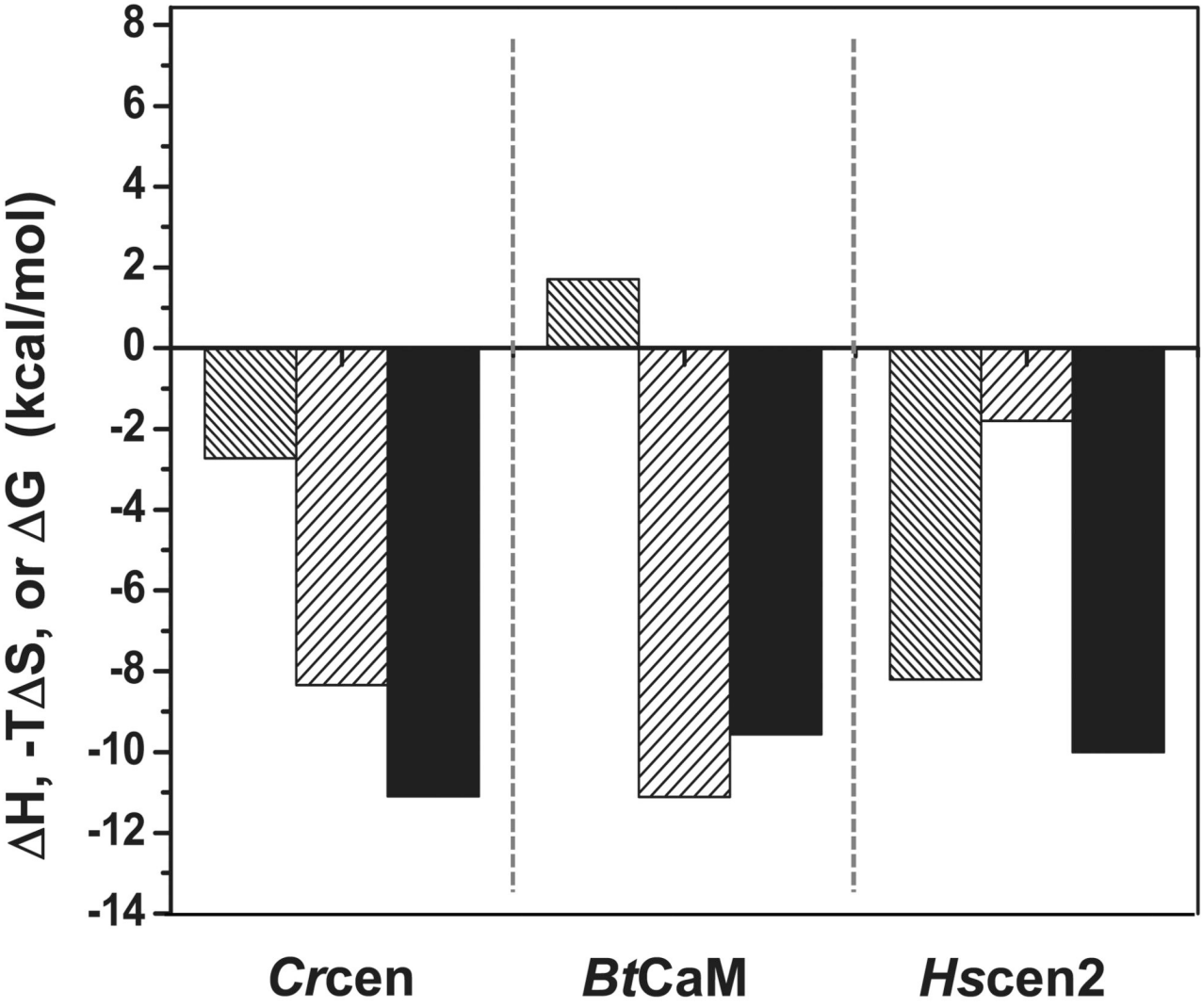

FIGURE 2.

Comparison of enthalpic (ΔH_b, narrow striped bars) and entropic ($-T\Delta S$, wide striped bars) contributions to Gibbs free energy (ΔG, solid bars) of CaBP-MLT complex formation at varying temperatures (25, 25, and 30°C) and pH (7.4, 7.0 and 6.5) for *Cr*cen (results presented herein), *Bt*CaM (14), and *Hs*cen2 (16); respectively.

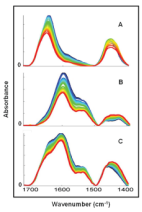

FIGURE 3.

Spectral changes in the region of 1720 – 1390 cm^{-1} as a function of temperature for (A) MLT, (B) ^{13}C-*Cr*cen, and (C) the ^{13}C-*Cr*cen-MLT complex (1:2, mol ratio); from blue (5°C) to red (95°C).

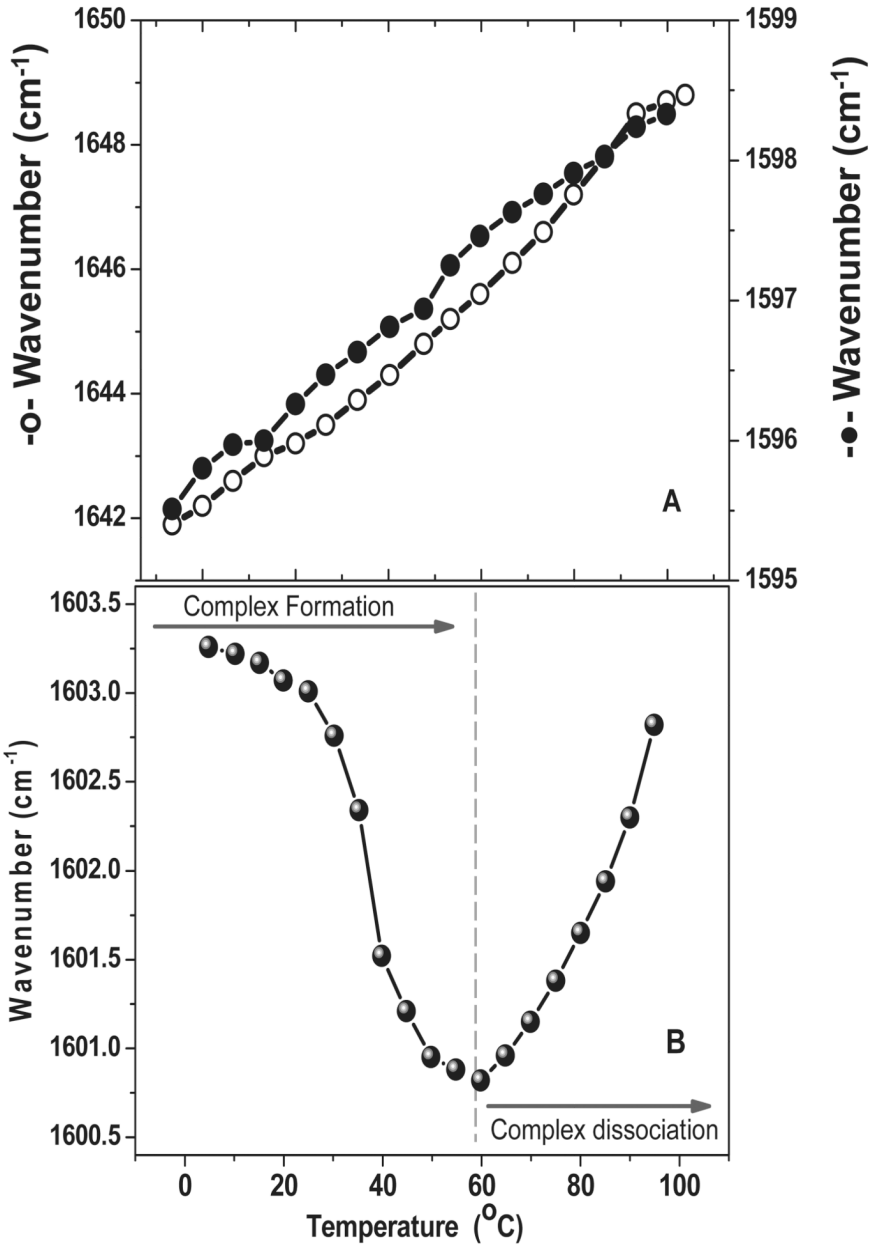

FIGURE 4.

Change in the maximum peak frequency for: (A) pure protein components (open circle) MLT's amide I' band and (asterisk) ^{13}C-*Cr*cen's amide I'* band, and (B) ^{13}C-*Cr*cen-MLT complex (1:2, mol ratio) amide I'* band; within the temperature range of 5–95°C. In the lower panel (B) the dash line separates the cooperative effect associated with complex formation within the temperature range of 5–60°C and that of complex dissociation which occurs within the temperature range of 60–95°C.

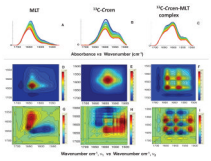

FIGURE 5.

The thermally induced spectral changes in MLT, ^{13}C-*Cr*cen, and ^{13}C-*Cr*cen-MLT complex (1:2 molar ratio) are shown as overlaid FT-IR spectra (A–C) and synchronous (D–F) and asynchronous (G–I) plots within the spectral region of 1720–1490 cm^{-1} and 5–95°C temperature range.

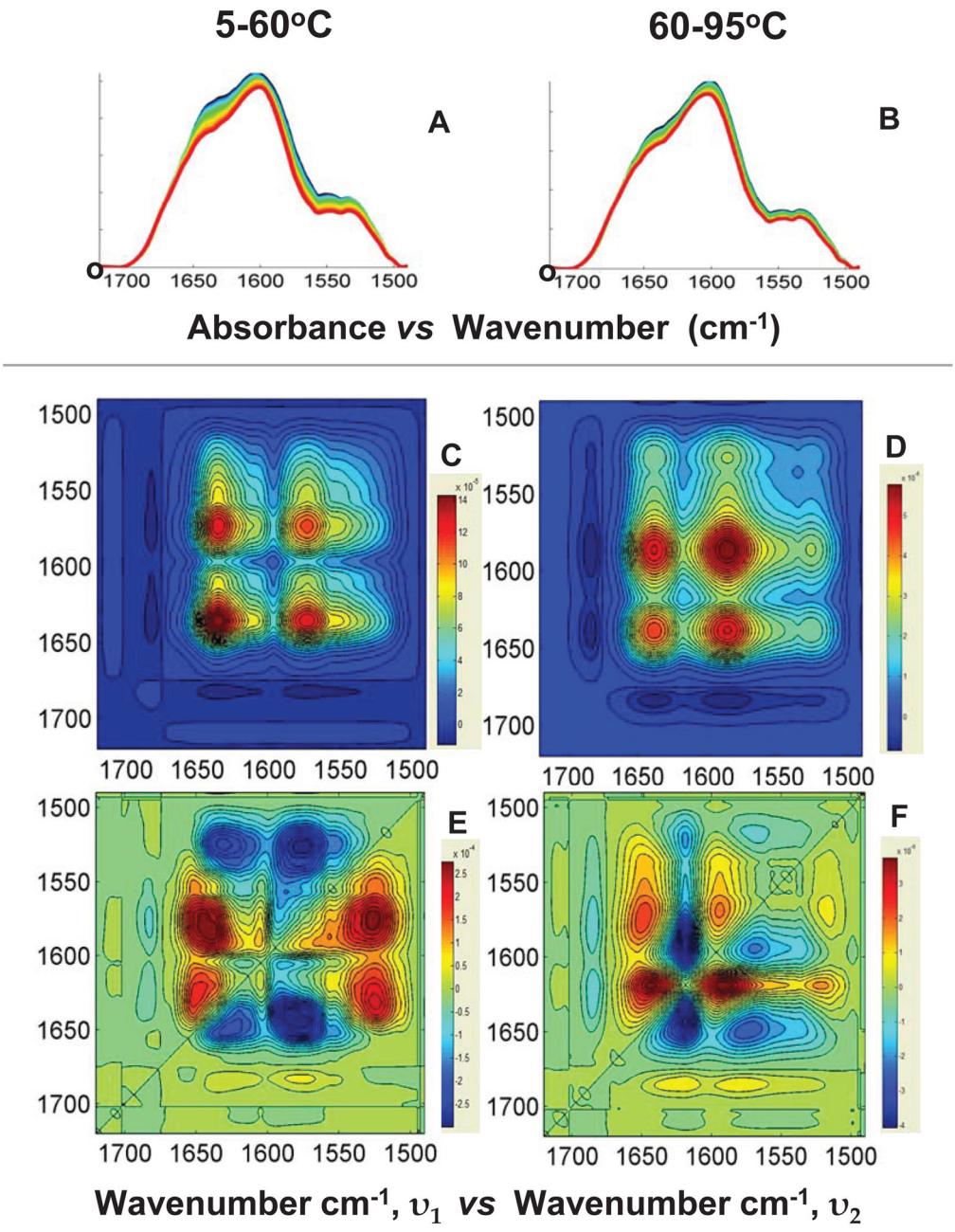

FIGURE 6.

The thermally induced spectral changes for ^{13}C-*Cr*cen-MLT complex (1:2 molar ratio) are shown as overlaid FT-IR spectra (A,B) and synchronous (C,D) and asynchronous (E,F) plots within the spectral region of 1720–1490 cm^{-1} for complex formation: **(A,C,E)** within the temperature range of 5–60°C and for complex dissociation **(B,D,F)** within the temperature range of 60–95°C.

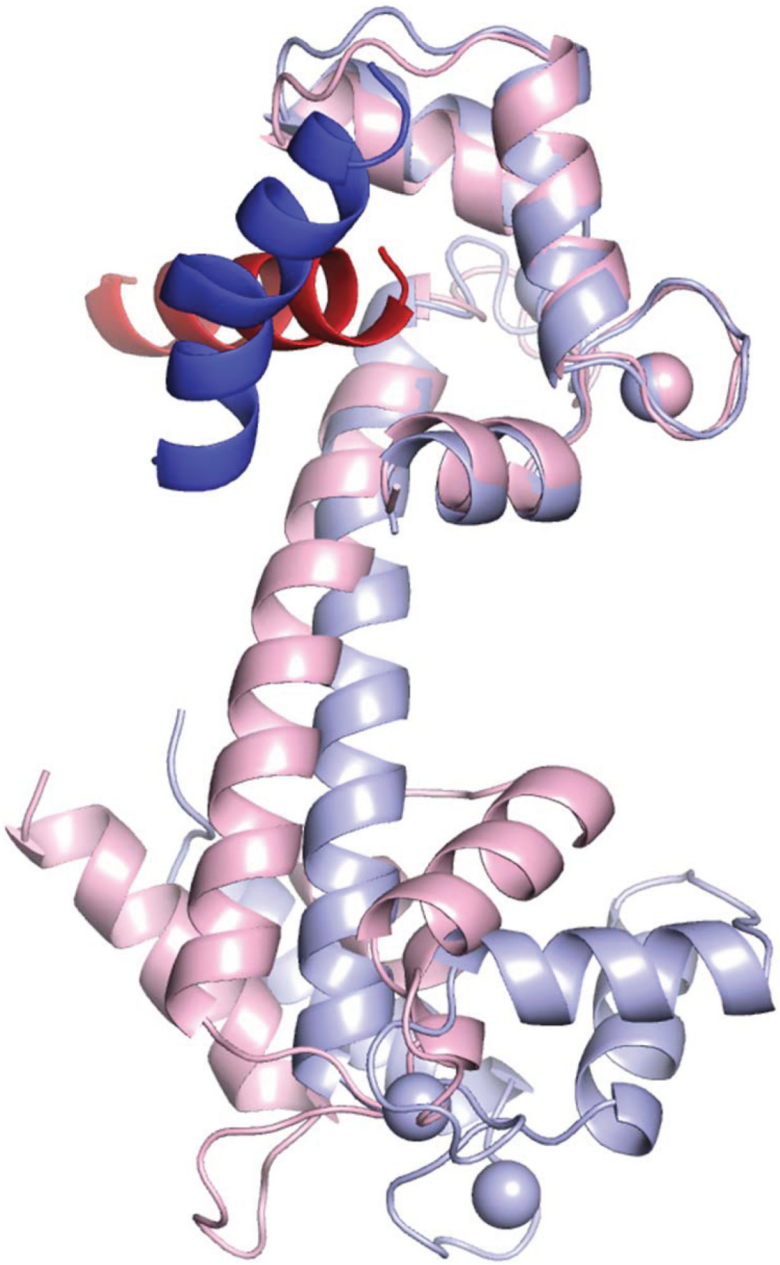

FIGURE 7.
Structural superimposition of *Chlamydomonas* reinhardtii centrin (light blue) bound to melittin (blue) with human centrin 2 (pink) bound to the XPC peptide (red). Fifty-six alpha carbons of the C-terminal domains of the proteins, located in the top portion of the ribbon diagram, were aligned (RMSD=0.868 Å) to illustrate the different interactions of the two peptides with centrin. Calcium ions are illustrated as pink or light blue spheres.

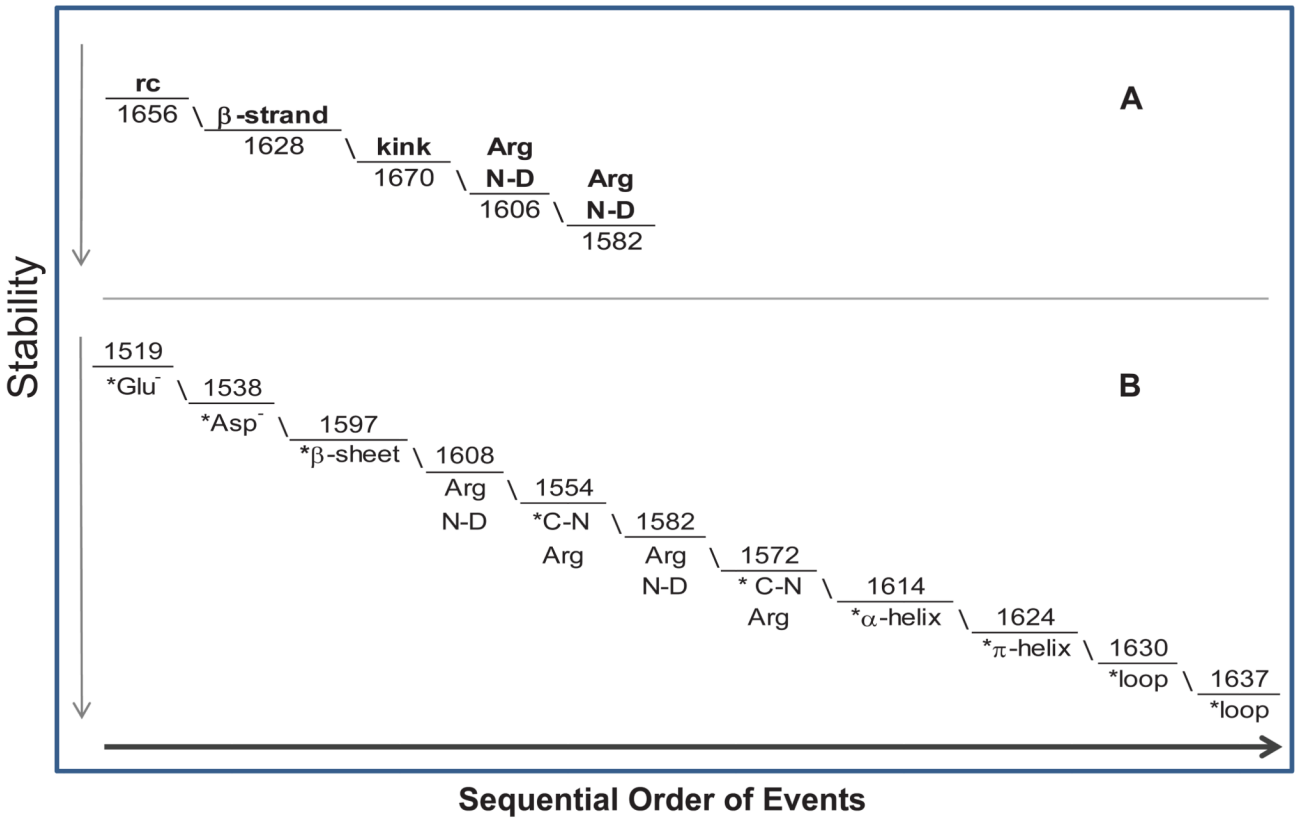

SCHEME 1.

Schematic representation summarizing the order of events during the thermal perturbation of the pure protein components (A) MLT and (B) ^{13}C-*Cr*cen.

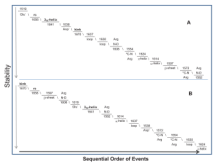

SCHEME 2.

Schematic representation summarizing the order of events of the thermally induced ^{13}C-*Cr*cen-MLT complex (1:2 molar ratio) (A) formation and (B) dissociation process.

Table 1

X-ray data collection and refinement statistics

Data Collection		Refinement	
Space Group	$P2_12_12$	Resolution (Å)	20–2.30
Unit Cell Dimensions		Number of Reflections	
a, b, c (Å)	52.08, 114.36, 34.82	$\boldsymbol{R_{work}/R_{free}}$	0.291/0.341
α, β, γ (°)	90, 90, 90	Number of Atoms/*B*-factors	1328/48.8
Wavelength (Å)	1.5418	Centrin	1157/45.4
Resolution Range (Å)*	20–2.30 (2.38–2.30)	Melittin	136/65.1
R_{sym}(%)*,†	6.5 (48.9)	Ca^{2+} Ions	4/37.1
$I / \sigma(I)$*	10.7 (3.9)	Waters	31/42.2
Completeness (%)*	97.3 (95.6)	**RMSD**	
Redundancy*	6.4 (6.2)	Bond Lengths (Å)	0.022
		Bond Angles (°)	1.753

* The number in parentheses is for the highest resolution shell.

† $R_{sym} = \Sigma^i_{hkl} | I^i(hkl) - \langle I(hkl) \rangle | / \Sigma_{hkl} \langle I(hkl) \rangle$, where $I^i(hkl)$ is the i^{th} measured diffraction intensity and $\langle I(hkl) \rangle$ is the mean of the intensity for the Miller index (*hkl*).